Research Article Vol. 58, No. 5 / 10 February 2019 / Applied Optics 1223

applied optics

Demonstration of resolving power $\lambda/\Delta\lambda > 10{,}000$ for a space-based x-ray transmission grating spectrometer

Ralf K. Heilmann,[1,*] Jeffery Kolodziejczak,[2] Alexander R. Bruccoleri,[3] Jessica A. Gaskin,[2] and Mark L. Schattenburg[1]

[1]Space Nanotechnology Laboratory, MIT Kavli Institute for Astrophysics and Space Research, Massachusetts Institute of Technology, Cambridge, Massachusetts 02139, USA
[2]NASA Marshall Space Flight Center, Huntsville, Alabama 35812, USA
[3]Izentis, LLC, Cambridge, Massachusetts 02139, USA
*Corresponding author: ralf@space.mit.edu

Received 11 October 2018; revised 18 December 2018; accepted 26 December 2018; posted 2 January 2019 (Doc. ID 347998); published 6 February 2019

We present measurements of the resolving power of a soft x-ray spectrometer consisting of 200 nm period lightweight, alignment-insensitive critical-angle transmission (CAT) gratings and a lightweight slumped-glass Wolter-I focusing mirror pair. We measure and model contributions from source, mirrors, detector pixel size, and grating period variation to the natural linewidth spectrum of the Al-$K_{\alpha_1\alpha_2}$ doublet. Measuring up to the 18th diffraction order, we consistently obtain small broadening due to gratings corresponding to a minimum effective grating resolving power $R_g > 10{,}000$ with 90% confidence. Upper limits are often compatible with $R_g = \infty$. Independent fitting of different diffraction orders, as well as ensemble fitting of multiple orders at multiple wavelengths, gives compatible results. Our data leads to uncertainties for the Al-K_α doublet linewidth and line separation parameters two to three times smaller than values found in the literature. Data from three different gratings are mutually compatible. This demonstrates that CAT gratings perform in excess of the requirements for the *Arcus Explorer* mission and are suitable for next-generation space-based x-ray spectrometer designs with resolving power five to 10 times higher than the transmission grating spectrometer onboard the Chandra X-ray Observatory.

https://doi.org/10.1364/AO.58.001223

1. INTRODUCTION

The soft x-ray band (roughly between 0.2 and a few keV in energy) contains many atomic resonances. Spectra in this band offer a wealth of diagnostics about the composition, density, and temperature of x-ray emitting or absorbing objects. In astronomy, important lines of highly ionized carbon, nitrogen, oxygen, neon, and iron can be found in the wavelength range between 1 and 5 nm. Emission and absorption line spectroscopy of celestial objects and structures in this band have the potential to provide essential information for the study of large-scale structure formation (galaxy clusters), feedback from supermassive black holes, hot gas in the cosmic web, and stellar evolution, i.e., information that is often not available at other wavelengths [1,2].

Soft x-rays are readily absorbed by small amounts of matter, which makes it difficult to build efficient transmitting optical elements, such as lenses or transmission gratings. Obviously, absorption by air requires us to study the x-ray universe from satellites above the Earth's atmosphere.

Spectroscopic information can be obtained using energy dispersive instruments, such as microcalorimeters [3] or grating spectrometers, which are wavelength dispersive. The energy resolution of microcalorimeters is typically on the order of a few eV (but can be sub-eV) [4], which gives $E/\Delta E \sim 200$–1000 for soft x rays. Similar resolving power $\lambda/\Delta\lambda$ can be obtained from existing but aging instruments onboard the *Chandra* (high-energy transmission grating spectrometer [HETG]) [5] and *XMM-Newton* (reflection grating spectrometer RGS) [6] x-ray observatories, both of which were launched in 1999. Their effective areas are rather small, in the range of a few tens to $\sim$100 cm^2, resulting in long observation times up to megaseconds (over one week for a single object). For many of the above science questions, $\lambda/\Delta\lambda > 2500$ is required, and $\lambda/\Delta\lambda > 5000$ is desired.

High-resolution soft x-ray spectroscopy has been demonstrated with laboratory sources and double-crystal spectrometers [7]. In the last two decades, much development has taken place at electron beam ion traps [8–11] and synchrotron sources, the latter mostly focusing on resonant inelastic x-ray scattering [12–17]. Dispersing elements are mostly crystals, plane, or variable-line-spacing reflection gratings. The spectrometers often achieve $\lambda/\Delta\lambda$ on the order of a few thousand to ~10,000. Many of these spectrometers depend on strong sources, precise and adjustable alignment, and multiple movable elements to achieve a broad bandpass. These designs would be difficult to implement in space, where movable elements and mass should be minimized.

Space-based x-ray grating spectrometers (XGS) are typically designed with an array of objective gratings just downstream of the focusing telescope mirrors (the "lens," usually a set of concentric Wolter-I grazing-incidence mirrors). Due to the sparseness of celestial x rays, mirrors should extend over a significant aperture on the order of 1 m^2, and gratings should cover a large part of or the whole mirror aperture. In the in-plane transmission geometry, where the grating vector connecting two grating bars lies in the plane of incidence, the gratings diffract photons incident at angle α relative to the grating normal into diffraction orders m at angles β_m according to the grating equation

$$\frac{m\lambda}{p} = \sin\alpha - \sin\beta_m, \quad (1)$$

where $m = 0, \pm 1, \pm 2, \ldots$, λ is the x-ray wavelength, and p is the grating period (see Fig. 1). The gratings are arrayed on the surface of a Rowland torus [18,19], such that the mth diffraction order from each grating comes to a common focus on the surface of a detector with fine spatial resolution, typically an x-ray CCD. For a broad spectrum, different orders from different wavelengths can overlap spatially. The resulting limited free spectral range $\Delta\lambda = \lambda/m$ can be overcome if the energy resolution of the detector is better than the corresponding photon energy difference ΔE, divided by m [20].

The resolving power of an XGS can be defined as

$$R_{XGS} = \lambda/\Delta\lambda, \quad (2)$$

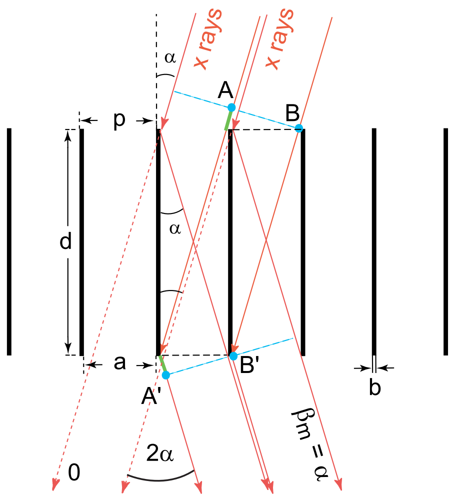

Fig. 1. Schematic cross section through a CAT grating of period p. The mth diffraction order occurs at an angle β_m, where the path length difference between AA′ and BB′ is $m\lambda$. Shown is the case where β_m coincides with the direction of specular reflection from the grating bar sidewalls ($|\beta_m| = |\alpha|$), i.e., blazing in the mth order.

where $\Delta\lambda$ is the smallest wavelength difference that can be resolved at wavelength λ. To the first order, R_{XGS} is given by the distance of the mth order spot on the CCD from the zeroth order divided by the width of the telescope mirror point-spread function (PSF) in the dispersion direction. It is therefore advantageous to use high diffraction orders and a small grating period and to have a narrow PSF. High diffraction orders are only useful if a large percentage of incident photons lands in these orders. This has been achieved via blazing with sawtooth groove profiles for grazing incidence reflection gratings [6,21–24]. However, the reflection geometry is sensitive to misalignments and grating non-flatness, and grazing incidence requires many cm long substrates with larger mass than μm thin transmission gratings.

Critical-angle transmission (CAT) gratings combine the advantages of the transmission geometry (alignment insensitivity, low mass) with efficient utilization of high diffraction orders (blazing) [20,25]. As shown in Fig. 1, this is accomplished by tilting freestanding ultrahigh-aspect-ratio grating bars by a small angle α, which is less than the critical angle for total external reflection, relative to the incident x rays. Diffraction orders near the direction of specular reflection from the grating bar sidewalls have enhanced diffraction efficiency. Thin grating bars ($b < p/3$) and lack of a support membrane minimize absorption. We have recently fabricated 200 nm period, 4 μm deep silicon CAT gratings up to 32×32 mm^2 in size, with blazed diffraction efficiency >30% at $\lambda \sim 2.5$ nm and >20% for 1.5 nm $< \lambda <$ 5 nm, [26] compared with ~1–5% for HETG gratings. [5]

At $\lambda = 1.5$ nm the critical angle for silicon is ~2 deg. If we set $\alpha = 2$ degrees, then we expect to blaze orders near $\alpha + \beta_m = 4$ degrees, i.e., 9th and 10th order. For a telescope with a PSF of 1 arcsec FWHM f_{PSF}, we expect $R_{XGS} \approx (\alpha + \beta_m)/f_{PSF} = 4°/1'' = 14400$ (neglecting that the gratings are slightly closer to the focus than the mirrors). However, XGS optical designs are neither free from aberrations nor will a real XGS follow its design perfectly. We have undertaken numerous ray-trace studies of transmission XGS designs to understand the limits of performance, alignment tolerances, and other imperfections [18,19,27–30] and concluded that instruments with $R_{XGS} \sim 10000$ and effective area >1000 cm^2 should be feasible in the near future.

XGS resolving power can be compromised by grating imperfections, such as variations in the grating period, described by some period distribution $\{p\}$ with FWHM Δp, for example. Equation (1) shows that, if $\Delta p \neq 0$, then there will be a distribution of diffraction angles $\{\beta_m\}$ with FWHM $\Delta\beta_m$ and a broadening of the mth order diffraction peak proportional to m. Neglecting aberrations, the observed peak broadening is then a convolution between the PSF and the β_m distribution function. Because $\Delta\beta_m$ scales with m, it can become the dominating source of broadening in higher orders and limit resolving power to a value less than $(\alpha + \beta_m)/f_{PSF}$. If we assume $\{p\}$ to be Gaussian, then R_{XGS} can never be greater than $p/\Delta p$. In our analysis, we simply model grating imperfections as a Gaussian period distribution and call $R_g = p/\Delta p$ the effective resolving power of the grating (see Fig. 2), which is different from the traditional definition of resolving power or resolvance of a

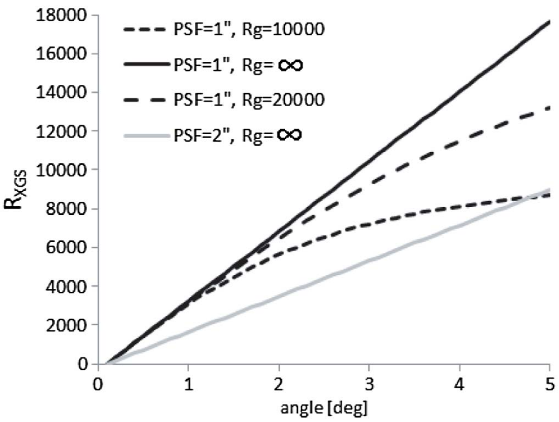

Fig. 2. Simple model of resolving power as a function of diffraction angle for an objective grating spectrometer with $f_{\mathrm{PSF}} = 1$ arcsec (black lines) and 2 arcsec (gray line). Solid lines represent no broadening due to the grating ("$R_g = \infty$"), while dashed lines show the impact of finite effective grating resolving power R_g.

grating, mN, where N is the number of illuminated grating lines. The present work was undertaken to study broadening of spectral features due to potential CAT grating imperfections that could limit resolving power in an XGS.

To mimic an XGS, we need a soft x-ray source with a narrow spectral line, a focusing optic with narrow PSF that can fully illuminate a grating of reasonable size, and a detector with high spatial resolution. At the time of this work, we were not aware of any synchrotron end-stations that could have provided us with an expanded, collimated beam and a 10 m long vacuum chamber and the necessary manipulators. For traditional laboratory soft x-ray sources, the narrowest lines are provided by the Al and Mg $K_{\alpha_1\alpha_2}$ doublets at $\lambda = 0.834$ and 0.989 nm, respectively, with $E/\Gamma \sim 3500$, where Γ is the FWHM of each of the K_α lines and E is the photon energy. For silicon, the critical angles for these wavelengths are only ~1.1 and ~1.35 deg. In order to obtain higher diffraction efficiencies at the highest orders possible, we coated some CAT gratings with a thin layer of platinum, effectively increasing the critical angle.

In the following, we first describe our experimental setup, then our measurements and models, and finally the results of fitting our models to the data. We then discuss our results and summarize our conclusions.

2. EXPERIMENTAL SETUP

The measurements were performed at the NASA Marshall Space Flight Center Stray Light Test Facility (SLTF). It consists of a 92 m long, 1.22 m diameter vacuum guide tube that opens into a 12.19 m long, 3.05 m diameter vacuum chamber (see Fig. 3). The far end of the guide tube connects to a Manson electron impact x-ray source. The source is equipped with 100 and 150 μm vertical slits to reduce the horizontal width of a 0.5 mm source spot, effectively improving the source size from 1.12 arcsec to 0.22 and 0.34 arcsec, respectively.

The grating spectrometer is part of an imaging system. In astronomical applications, an ideal point source at infinity is imaged to a small spot in the focal plane of a focusing optic.

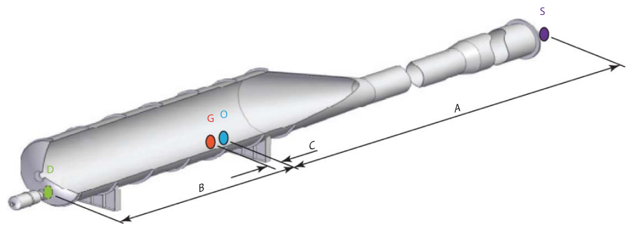

Fig. 3. Overall configuration of the SLTF for this test, depicting the locations of S-source, O-optic node, G-grating, and D-detector. The source-to-optic-node distance A is 92.17 m. The detector-to-optic-node distance B is 9.25 m. The grating-to-optic-node distance C is 0.50 m.

The image of the point source is broadened due to the finite angular width of the optic PSF. In order to separate spectral features with a small $\Delta\lambda$, a sufficiently small PSF is required. In this work, we used an 8.4 m focal-length technology development module (TDM) [31] manufactured by the Next Generation X-ray Optics group at the NASA Goddard Space Flight Center. The TDM consisted of two 0.4 mm thick Wolter-I slumped glass segments: a gold-coated parabolic (P) segment, followed by an iridium-coated hyperbolic (H) segment. The radius at the node of the optic, i.e., the center between the P and the H segments, was 245 mm, the azimuthal extent 30 deg, and each glass segment was about 200 mm long along the optical axis or z direction (see Fig. 4). The half-power diameter (HPD) of the 2D PSF of a single mirror-pair TDM is typically about 8 arcsec and the coating roughness about 0.5 nm. Due to the finite source distance, the best focus of

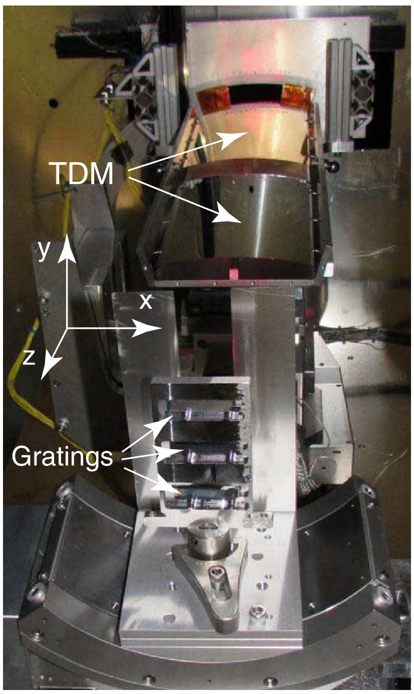

Fig. 4. Picture of the experimental setup. The mount with the three gratings is seen in the foreground, followed by the 30 mm grating mask, the Ir- and Au-coated TDM mirrors, and the optics mask.

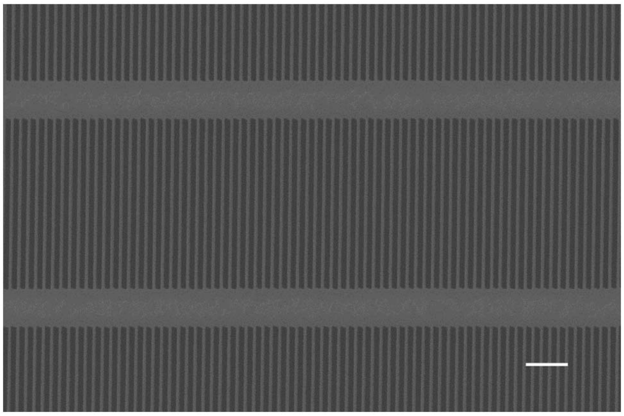

Fig. 5. Top-down scanning electron micrograph of grating X7, showing the 200 nm period CAT grating bars and the 5 μm period L1 cross-support mesh. The scale bar is 1 μm long.

the source is obtained 9.25 m from the optic node. The optic was mounted on a stage stack for pitch (rotation around x or the horizontal axis) and yaw (rotation around y or the vertical axis) alignment. Upstream of the optic was a large plate to block direct illumination of the focal plane by the source and a selectable aperture plate for the TDM.

Three different CAT gratings were used in this work. They were all fabricated from silicon-on-insulator (SOI) wafers. Freestanding CAT grating bars with a 200 nm period were etched out of the nominally 4 μm thick SOI device layer at the same time as a 5 μm period Level 1 (L1) cross-support mesh (see Fig. 5), using a combination of deep reactive-ion etching (DRIE) and wet etching in a potassium hydroxide solution. A coarse Level 2 (L2) hexagonal support mesh (~1 mm pitch) was etched out of the 0.5 mm thick SOI handle layer. The buried oxide layer separating device and handle layers has been removed from the open areas between the etched structures. Details of the fabrication process can be found in [32–36]. The usable grating area was 32 mm long and between 5.7 and 7.5 mm wide, depending on the grating. Gratings X1 and X4 were nominally coated with 2 nm of aluminum oxide and 7 nm of platinum using atomic layer deposition. Grating X7 was left uncoated (see Fig. 6).

The gratings were mounted in a vertical stack in a holder 50 cm downstream of the TDM node, with their long axes in the horizontal direction (see Fig. 4). The holder was mounted on a stage stack consisting of a linear x-translation

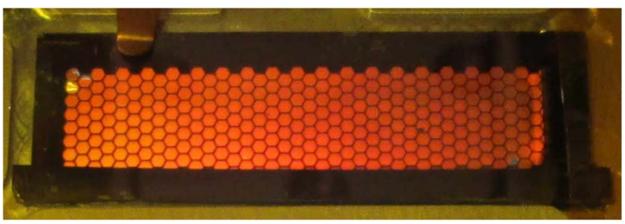

Fig. 6. Picture of grating X7. The device layer is partially transparent, making the back-lit hexagonal L2 support mesh visible. The L1 and L2 support structures combined occupy about 34% of the grating area.

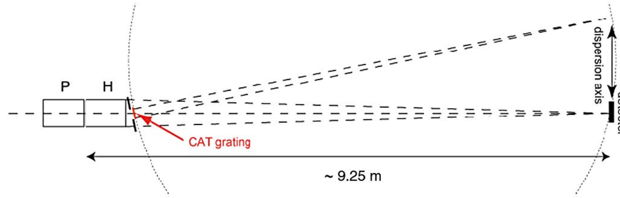

Fig. 7. Planview of the experimental layout (not to scale). X rays are incident from the source from the left. The dotted circle shows a cross section of the Rowland torus.

stage at the bottom that carried a yaw stage, followed by y-translation and roll (rotation around optical axis) stages. The whole stack was tilted in pitch by ~1.4 deg to achieve close to normal x-ray incidence on the gratings. Just upstream of the gratings, we placed an aperture mask that limited the grating illumination to 30 mm in the horizontal direction. The converging x-ray beam incident on a grating thus had a cross section in the shape of a shallow arc of about 1.5 mm in the radial extent and about 30 mm in the azimuthal direction and 242 mm radius of curvature.

The detector was a model DX436-BN-9HS CCD from Andor Corp. The imager consisted of 2048×2048 pixels (13.5 μm pixel pitch) with settable clocking speeds. The array was covered by an optical blocking filter consisting of 150 nm Al on 200 nm polyimide. Needing minimal energy resolution, we ran at the fastest clocking speed of 1 μs per pixel during the test. The detector was mounted on a three-axis xyz stage stack. The detector operating temperature was maintained at a constant -45°C for the entire test.

Before evacuation of the chamber, we performed preliminary alignment of the optics, gratings, and masks using a He–Ne laser at the source end. The TDM was placed 245 mm above the horizontal optical axis with its reflective sides facing down. A second laser, aimed from the optics focus back toward one of the gratings, was used to visualize the orientation of the L1 mesh dispersion axis. We rolled the grating mount until this axis was vertical, thus placing the CAT grating dispersion axis close to horizontal orientation. The gratings therefore disperse close to the direction along which the anisotropic optic PSF is expected to be at its narrowest. A schematic of the experimental layout is shown in Fig. 7.

3. MEASUREMENTS

We first characterized the direct ("unobstructed") beam from the TDM, and, after grating insertion, the beam transmitted straight through the gratings (0th diffracted order). Following this, we explored higher diffraction orders until hardware limitations prevented us from going further.

Dark images (with the source shutter closed) were collected periodically to monitor the dark levels produced by the camera readout electronics. The first images of the optic under Al-K illumination gave a sufficiently narrow PSF. We did not perform any further pitch and yaw fine adjustment of the optics with x rays until the end of this study. The best focus was found through a series of images taken at different camera positions along the optical axis.

A. Combined Performance of Source, Mirror, and Detector

The focal spot from the TDM (direct beam) exhibits a narrow "hour-glass" or rotated "bow-tie" cross section whose dispersive-direction (x) FWHM varies as a function of cross-dispersion direction coordinate (y) [see Fig. 8(a)]. This so-called subaperture effect is a well-known feature of reflection at small angles of grazing incidence from surfaces of finite roughness [18,30,37]. The measurement is the result of the convolution of the source size, mirror PSF, and finite CCD pixel size. The mirror performance is estimated from images taken under three-source slit configurations. The open (no slit), 150 μm, and 100 μm configurations produce sources with FWHMs of 0.97, 0.33, and 0.22 in. in the dispersion direction, respectively, indicating a 0.43 mm source spot width. The source spot extends 1.2 arcsec. in the cross-dispersion direction in all cases.

Due to the irregular shape of the beam image, we define a series of cross-dispersion bands (CDBs). These CDBs are a rebinning of images into nine 21-pixel vertical bands extending from −94 to +94 pixels from the narrowest region of the bow-tie. We define the term "line profile" as the 1D measured distribution of detected charge in the dispersion direction integrated (or binned) over some range in cross-dispersion direction. Figure 8(b) shows an image transformed to a binned image along with a series of line profiles in various CDBs [Fig. 8(c)]. Figure 9 is a plot of the measured FWHM versus CDB for a representative set of images taken at different times. The central five bands are consistent and were used in our modeling. The remaining bands (not shown), representing poorer regions of the mirrors, varied significantly over time. Temperatures in this region of the chamber typically vary by several degrees F during the course of the day, and we

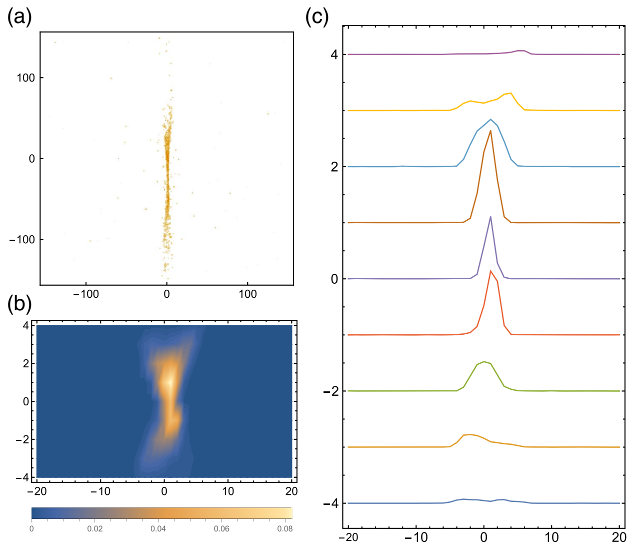

Fig. 8. Conversion of unobstructed beam image to line profiles for 100 μm slit data. (a) Original image showing "bow-tie" structure of mirror PSF. (b) Image recentered and rebinned into nine bands around the minimum FWHM. Each band is 21 pixels tall. (c) Stacked and relatively normalized line profiles for each band. The band with the smallest FWHM does not have the highest flux in this case.

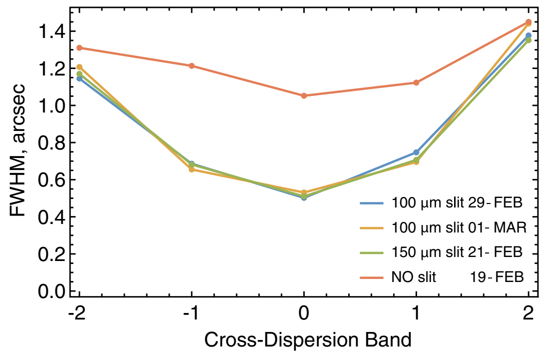

Fig. 9. Measured line profile FWHM versus CDB for unobstructed images obtained with the indicated slit configurations on indicated dates. The effect of the 100 μm slit, in comparison with the 150 μm slit is negligible, both being 0.50″ at minimum. The minimum FWHM for the no-slit configuration was 1.05″. 1σ errors of these values are less than 0.05″.

conjecture that regions of the optics, which have larger slope errors, e.g., the ends and regions near mounting supports, are more thermally sensitive. The rotation angle of the bow-tie relative to the CCD columns (fit over the five central CDBs) is <0.4 deg. Both slits, combined with the 0.30 in. pixel width, produce nearly indistinguishable line profiles when convolved with the mirror PSF, and there was no benefit in using the narrower slits.

From Fig. 9 and the grating equation, we can estimate R_{XGS}, neglecting any potential broadening from the gratings. For characteristic Al-K$_\alpha$ radiation in the 18th order, one obtains $R_{XGS} \sim 17200$ when using all five central CDBs. However, R_{XGS} can be increased to ~24000, for example, simply by utilizing only the three central CDBs, at the cost of losing counts and increasing statistical uncertainty. In principle, the same trade-off between effective area and resolving power can be exercised post-observation in the analysis of data from a space-based x-ray spectrometer.

We also examined the wings of the line profiles, which we can later evaluate for additional scattering introduced by the gratings. At grazing incidence surface roughness produces primarily in-plane scattering; the out-of-plane scattering, i.e., along the grating dispersion direction, can be dominated by particulate contamination on the mirror surfaces [38,39]. Figure 10 indicates that the cumulative distribution function (CDF) of the scattering distribution is consistent among all the slit configurations and CDBs and that it can be modeled by a Lorentzian function. From this model, we estimate that <5% of the flux is scattered beyond 5 pixels (or 1.5 arcsec.) along the dispersion direction.

B. Mirror Line Response

Knowing the contribution of source slit width or effective spot size and detector pixel size to the line profile, we can back out the mirror response by root difference of squares. The so-derived FWHMs and half power widths (HPW) are included in Table 1. The change with cross-dispersion is simply a function of the bow-tie wedge angle, due to the 7° angular extent of the used aperture; 84% of the flux is fairly evenly distributed

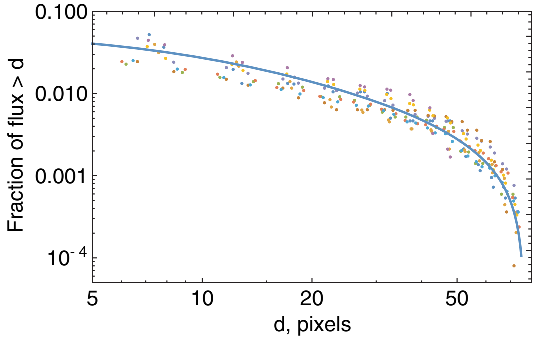

Fig. 10. Scatter plot of cumulative distributions of scattering along the dispersive direction from various band/slit combinations from the sets $\{\pm 2, \pm 1, 0\}$ bands and $\{150\ \mu m, 100\ \mu m, \text{open}\}$ slit. The solid curve is a Lorentzian function with FWHM = 20 pixels. The plot indicates that ~4% of the flux is scattered in the range 5 to 75 pixels, and we estimate roughly another ~0.5% outside of 75 pixels.

Table 1. Mirror Line Response in Three CDBs[a]

Cross-Dispersion Range Arcsec (pixels)	Line FWHM Arcsec	Half Power Width Arcsec	Flux Fraction in Range %
<3.16 (<10.5)	0.40 ± 0.01	0.27 ± 0.01	15
3.16–9.48 (10.5–31.5)	0.61 ± 0.03	0.41 ± 0.02	36
9.48–15.80 (31.5–52.5)	1.23 ± 0.12	0.84 ± 0.08	33

[a]FWHM, half-power width, and fractional flux are listed for the central five CDBs. The results from each of the ±1 and ±2 CDBs are averaged, and differences are included in the errors. The half-power width along the cross-dispersion direction is 19″, and 84% of flux is within the central five CDBs.

among the five central CDBs, while 15% is in the central band. The cross-dispersed flux distribution was double-peaked, so at best focus the two peaks straddled the center of the bow-tie, leaving a lower intensity at the center. (Small TDM realignment near the end of testing eliminated the double-peak and increased the flux in band 0 by >50%.)

C. Estimated Flux and Effective Area

We have previously measured the x-ray flux from the Manson source with the same detector on several occasions and obtained repeatable results. Based on facility geometry, anode voltage, slit settings, and measured count rates in the Al-K_α band through the TDM, we find an effective area of 0.36 cm^2 for the mirror pair. This is about 90% of the geometric aperture, consistent with 95% reflectivity per mirror, and slightly high compared with theoretical reflectivities (92%–93%). However, we estimate at least 5% uncertainty for this measurement.

D. Zeroth Order Profiles

The zeroth order line profiles are insensitive to narrow features in the source spectrum. They were measured to investigate any nondispersive effects the gratings may have on the line profile.

The vertical stage on the grating stage stack was used to move gratings in and out of the beam, and the beam was

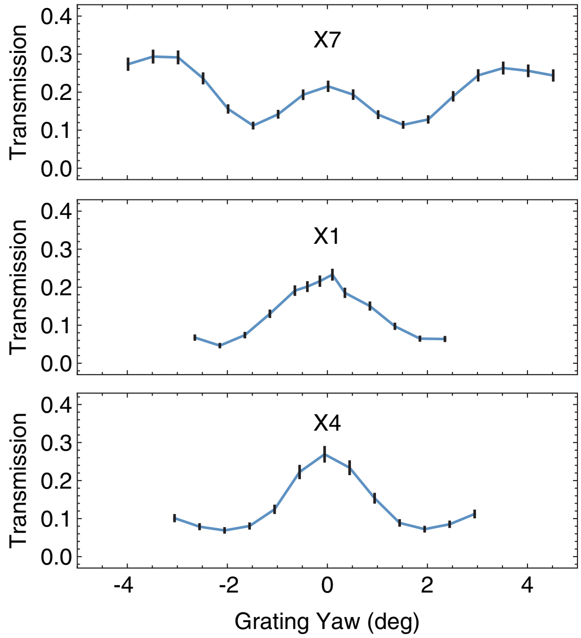

Fig. 11. Measured transmitted zero-order diffraction efficiency as a function of grating yaw for the three gratings. Curves are shifted to place the central maximum at zero. Maximum transmission values at zero yaw were X7:0.22 ± 0.01, X1:0.23 ± 0.01, and X4:0.27 ± 0.02.

centered on the grating during illumination. For blazed gratings, the efficiency of diffracted orders is sensitive to alignment [20,25,40], which can vary between gratings due to our mounting method. We thus measured the zero-order flux as a function of yaw angle (rotation around an axis parallel to the grating bars and the grating surface, which sets the blaze angle). For ideal CAT gratings, this function is symmetrical around the angle of normal incidence. Figure 11 shows measured zero-order efficiency for all three gratings, offset in yaw to center the curves on zero degrees. Differences between the gratings are due to small differences in average grating bar widths and device layer thickness as well as the Pt coating for gratings X1 and X4.

1. Comparison with Mirror-Only and Among Gratings

Zeroth order line profiles were measured with each grating at its own (yaw = 0) position. The profiles of all three gratings were identical within measurement uncertainty. For the 100 μm slit configuration for the central CDB, where the line profile is the narrowest, a simple Gaussian model was fit to each separate data set, and the width parameters were converted into FWHM. The FWHMs in arcsec are $X4: 0.50 \pm 0.02''$, $X1: 0.45 \pm 0.06''$, and $X7: 0.47 \pm 0.04''$. Compared with $0.47 \pm 0.01''$ for the unobstructed beam, we see no broadening from the gratings.

To compare scattering from the gratings, we looked at the wings for the central five CDBs in the 100 μm slit configuration. For comparison, we take the ratio of flux in the range of 5 to 75 pixels from the peak (in the x direction) to that within 75 pixels of the peak, similar to the analysis for the mirror line response in Fig. 10. The RMS variation between the gratings in this flux fraction is 1.0%, compared with 0.5% RMS of measurement errors.

The zero orders have higher scattering than in the unobstructed case. However, the amount of increased scatter is only 1.5% (X4, X7) and 3.5% (X1), so the contribution to the HPW is still small. For example, a 1 arcsec. HPW optic would have a 1.07 arcsec. zero-order HPW if the grating contribution to scattering is 3%.

2. Zeroth Order Line Response Function Model

We developed an empirical model for the zeroth order line response function (LRF) for the source/optic/grating/detector system, consisting of the sum of contributions of two Gaussians of different widths to describe the central core and a Lorentzian function (Cauchy distribution) to account for scattering. The model includes integration over the slit width and the pixel width. We simultaneously fit the data from 100 and 150 μm slit configurations in the five central CDBs. To simplify, we combined data from the ±1 bands as well as the ±2 bands. Figure 12 compares the fit with data points for the centermost CDB. The log-log plot emphasizes the scattering wings. In Section 4, we convolve the LRF with the expected source line spectra to generate the predicted response for dispersed orders.

E. Dispersed Line Profiles

We collected CCD images at numerous dispersed orders of the K_α doublet. In order to maximize the count rate for each measured order, we want to align the grating for most efficient blazing for each order separately. Blazing is strongest for orders under the blaze envelope, which is centered on the direction of specular reflection from the grating bar sidewalls, and has an angular width described by the distance between minima of diffraction w from a single slit of width a, the gap between bars, as $w \approx 2\lambda/a$ [20,25,40]. Therefore, the gratings were rotated in yaw from normal incidence by half the angle of the dispersed order in an effort to maximize blazing. For each order, the camera was also translated along the optical axis relative to the 0th order best focus to follow the expected best focus position (see Fig. 7). Figure 13 is a collage of all the orders measured on one side of the 0th order, scaled to a common maximum. Orders 7, 10, 14, and 18 were integrated for long times. By far, the longest integration was for the 18th order at 1726 min. It is easily seen that higher orders have progressively broader peaks, making it easier to observe spectral features and to deconvolve the source spectrum from the LRF. If we simply sum along the detector columns, we obtain the line profiles shown in Fig. 14. Orders 14 and 18 clearly show the well-known $K_{\alpha1,\alpha2}$ 2:1 intensity-ratio double-peak shape.

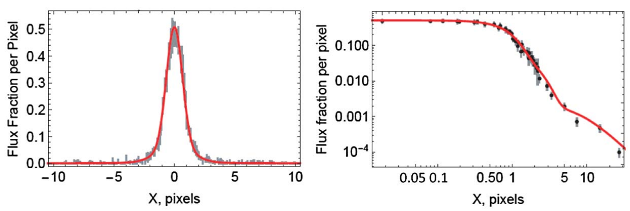

Fig. 12. Example best fit LRF model (solid line) compared with data for the 100 μm slit, CDB 0 case. The right figure shows the absolute value of X plotted against the flux fraction per pixel on log-log scales to emphasize the scattered component. Sparse wing data have been binned to produce ~10% error bars, and X positions are the centroids of data within each bin.

4. LINE MODELS AND GRATING EFFECTIVE RESOLVING POWER ANALYSIS

To estimate grating effective resolving power, we modeled the fluorescent lines emitted by the source anode using literature values for measured linewidths and wavelengths and applied the grating equation. When convolved with the zero-order line profiles, the resulting diffracted profiles constitute a measurement prediction for an ideal grating. Observed deviations from this model are interpreted as grating-induced. We initially model grating-induced broadening as a Gaussian grating period distribution.

A. Line Models

The line purity from the Al anode did not require additional modeling beyond the expected $K_{\alpha1}$ and $K_{\alpha2}$ lines. For reference, we compiled Al-K line energies and widths from various references in Table 2. In Fig. 15, we show the pure Al-K doublet line profile based on values and uncertainties from Table 2. We are constrained in trying to deduce the CAT grating effective resolving power by the intrinsic linewidth uncertainty, regardless of the precision of the measurement. For example, from [43] the intrinsic resolution of the Al-K lines is 3540 with linewidth uncertainties of 5%. A grating that causes the measured linewidth to exceed the natural linewidth by 5% would have an effective resolving power of 16000. Attempting to attribute a deviation from the known value to uncertainty in the known value or to grating performance, we cannot rely

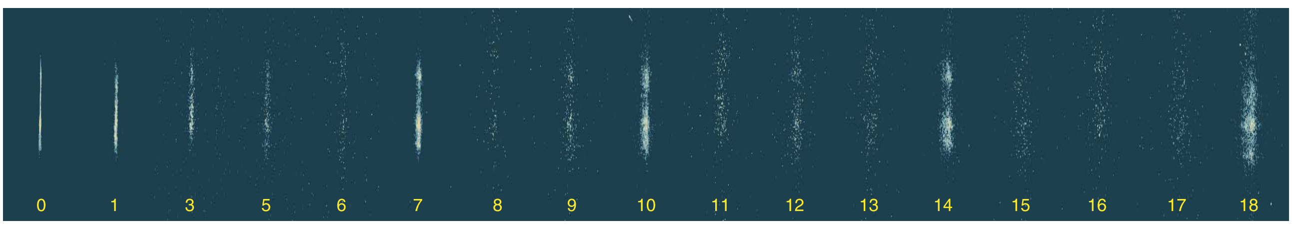

Fig. 13. Composite rebinned image of all orders collected using the Al anode. Orders 7, 10, 14, and 18 are long integrations. To make the images more visually comparable, pixel brightness is rescaled to the peaks of each rebinned image. No images were taken at orders 2 and 4. First order corresponds to the resolving power of the Chandra HETG at this wavelength.

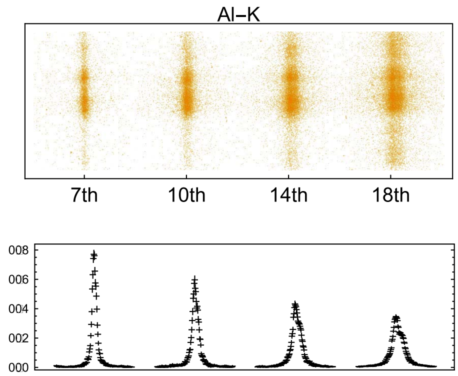

Fig. 14. Composite image of deep integration diffraction peaks collected for orders 7, 10, 14, and 18 using the Al anode. Pixel brightness has been rescaled, but images are at full resolution (no binning). Line profiles are derived from simple column sums and normalized to unity.

Table 2. X-ray Lines[a]

α_1		α_2		
λ	Γ	λ	Γ	Ref.
0.8339527 ± 0.0000056	0.4 ± 0.1	0.8341843 ± 0.0000056	0.4 ± 0.1	[7] (1994)
0.833934 ± 0.000009		0.834173 ± 0.000009		[41] (1967)
0.83393 ± 0.00006				[42] (1964)
	0.42 ± 0.02		0.42 ± 0.02	[43] (2001)
	0.43 ± 0.04		0.43 ± 0.04	[44] (1979)

[a]Line wavelengths, λ, (nm) and widths, Γ, (eV) from various references.

on broadening alone but need to discriminate between profile shapes.

The K_α doublets are modeled in the following manner: We assume that the naturally occurring energy distribution of photons around the line energies follows a Lorentzian function or Cauchy distribution described by

$$L_0(x, a, b) = \frac{1}{\pi b\left(\frac{(x-a)^2}{b^2} + 1\right)}, \tag{3}$$

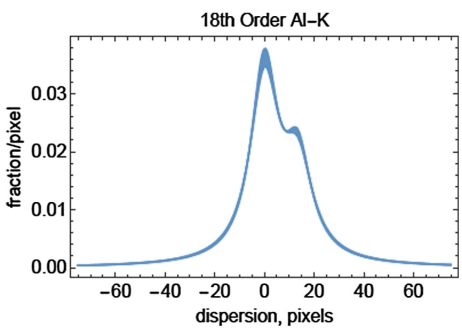

Fig. 15. Predicted Al-$K_{\alpha 1}$ and $K_{\alpha 2}$ lines without instrument effects. The plotted trace widths represent $\pm 1\sigma$ uncertainties in the line separation and characteristic linewidths, based on Table 2.

Table 3. Nominal As-Modeled X-ray Linewidths and Separations[a]

Model Constants	Nominal Values	Description
$\Gamma_{\alpha 1} = \Gamma_{\alpha 2}$	236 fm, 0.42 eV	Al $K_{\alpha 1}$, $K_{\alpha 2}$ Lorentzian FWHM
$\lambda_{\alpha 2} - \lambda_{\alpha 1}$	232 fm (0.413 eV)	Al $K_{\alpha 1}$, $K_{\alpha 2}$ separation

[a][7,43] We assume the equivalencies listed in the first column. The wavelength unit, fm, is femto-meters (10^{-15} m). For comparison, 1 pixel at orders $\{7, 10, 12, 14, 18\}$ extends over $\{44.05, 30.83, 25.70, 22.02, 17.13\}$ fm in wavelength space.

with FWHM $= f_L = 2b$ and peak at $x = a$. For comparison with data, we integrate L_0 across a pixel width, which is the scale at which we bin the integrated charge. Operationally, the function used is

$$L_1(x, a, b, d) = \frac{\tan^{-1}\left(x - a + \frac{d}{2}\right) - \tan^{-1}\left(x - a - \frac{d}{2}\right)}{\pi}, \tag{4}$$

where d is the width of the integration bin in the same units as a and b. We maintain pixels as the dispersion distance units throughout the analysis, converting only for certain figures. We define wavelengths relative to Al $K_{\alpha 1}$ in our line models. We have extracted nominal values for the necessary physical constants from Table 2 and listed them in Table 3. The modeled width and separation parameters are normalized relative to these nominal values. Setting all of these model parameters to 1.0 gives the nominal model.

Our model for the ith order Al $K_{\alpha 1}$, $K_{\alpha 2}$ lines is

$$\begin{aligned} &\mathbf{Al}_0(x, i, x_0, L, S, d) \\ &\quad = (2/3)L_1\left(x, x_0, \frac{f_{\alpha 1}}{2}, d\right) \\ &\quad\quad + (1/3)L_1\left(x, x_0 + \Delta_{\alpha 1,2}, \frac{f_{\alpha 2}}{2}, d\right) \\ f_{\alpha 1} &= i\kappa L \Gamma^A_{\alpha 1} \\ f_{\alpha 2} &= i\kappa L \Gamma^A_{\alpha 2} \\ \Delta_{\alpha 1,2} &= i\kappa S(\lambda^A_{\alpha 2} - \lambda^A_{\alpha 1}), \end{aligned} \tag{5}$$

where x is the dispersion axis coordinate, x_0 is the center position of Al $K_{\alpha 1}$, L is the fraction of the nominal Lorentzian FWHM, S is the fraction of the nominal line separation, and d is the bin width in units defined by κ. $f_{\alpha 1}$ and $f_{\alpha 2}$ are as-modeled Lorentzian FWHMs for the two lines, which are assumed equal. κ is a scale factor to convert wavelength to detector distance. $\Gamma_{\alpha 2}$ and $(\lambda_{\alpha 2} - \lambda_{\alpha 1})$ are defined in Table 3. The normalization yields 1.0 for the sum of points calculated at interval d. We have assumed that the flux ratio for $K_{\alpha 1}/K_{\alpha 2}$ is 2.

B. Measurement Model

The measurement model relates the line models to the measured integrated charge profile detected by the camera. The ingredients are the modeled line shapes, the grating dispersion relation, the zeroth order LRF, and the modeled dispersed grating response, assumed to be Gaussian.

We define a measurement model $\mathbf{Al}_\rho$, where ρ identifies the cross-dispersive region of interest in terms of the number of CDBs, as defined in Section 3.A. We combine data from various CDBs cumulatively in terms of distance from the center. Three values of ρ are considered initially:

$$\rho = 1 \quad \text{CDB:}\{0\},$$
$$\rho = 3 \quad \text{CDB:}\{0, \pm 1\},$$
$$\rho = 5 \quad \text{CDB:}\{0, \pm 1, \pm 2\}.$$

To go from function $\mathbf{Al}_0$ to $\mathbf{Al}_\rho$, we scale $\mathbf{Al}_0$ to the proper dispersion units, then convolve it with the appropriate zero-order LRF for the given ρ, and finally convolve it with a normalized Gaussian (FWHM f_G) representing the dispersed grating response.

We derive the dispersion relation in two ways: first, from the known grating period and measured grating-to-detector distance and, second, from the detector stage translation and CCD image positions. For the first, with a 200 nm grating period and a distance of 8750 ± 5 mm, we obtain 43.750 ± 0.025 mm/nm. For the 18th order, we measured a separation from zeroth order of 657.15 ± 0.1 mm, which gives 43.777 ± 0.007 mm/nm in the first order. We use 43.777 mm/nm or $\kappa = 3242.74$ pixels/nm and conclude that the 0.02% error is negligible, especially compared with ~5% uncertainty in the natural linewidths. We also use the notation for dispersion distance $D_m = m\kappa\lambda$, where λ is the $K_{\alpha 1}$ wavelength.

Figure 16 indicates the effect of the zero-order LRF and various levels of f_G on the line profile for 18th order.

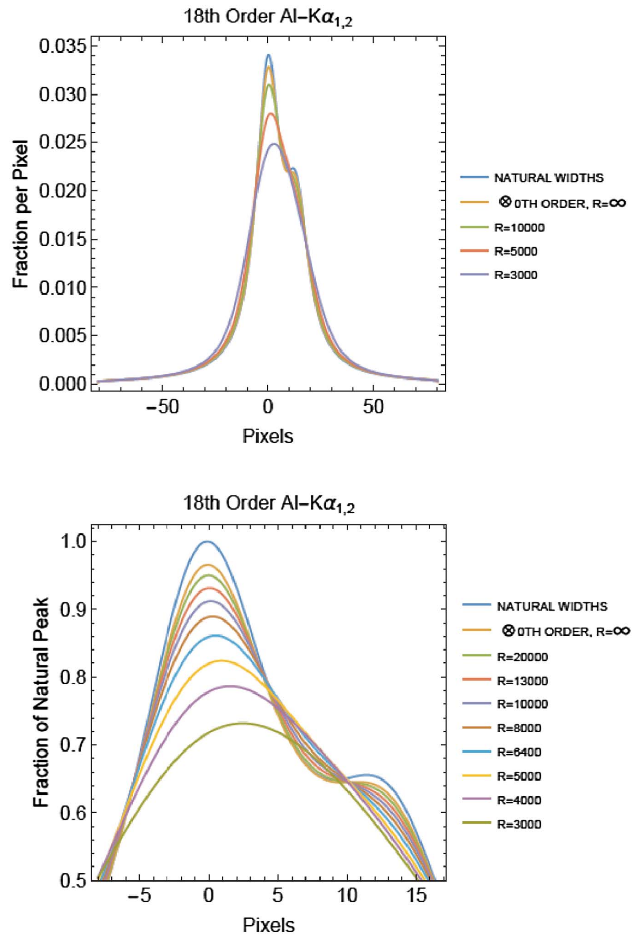

Fig. 16. Illustration of the measurement model for 18th order Al. Top panel shows the full profile at coarsely sampled effective resolving powers. Bottom panel shows the core region at finely sampled effective resolving powers.

C. Grating Effective Resolving Power Analysis

We performed independent fits to individual diffraction orders to estimate f_G and resolving power as well as fits to ensembles of orders. Fit analysis for the 18th order is described in detail. Analysis of other orders and ensembles is done in a similar fashion.

1. 18th Order

The 18th order data was fit in two stages: first, with only f_G variable, and then with all parameter variables. In the first stage, we separately fit the full profile and the core region interior to the FWHM, to explore possible systematic biases. For all of these cases, the model is

$$Q_\rho(x;\Phi) = Q_0 + n\mathbf{Al}_\rho(18, L, S, f_G)(x - x_0), \qquad (6)$$

with parameters listed in Table 4. Q_0 represents any continuum from other orders. $\mathbf{Al}_\rho$ is the measurement model for ρ CDBs.

The spectrum was first fit with wavelengths and linewidths fixed at their nominal values from Table 3 but with variable Gaussian FWHM. Best fit models for the $\rho = 1$, 3 and 5 cases were compared, using wide (143 pixels) and narrow (27 pixels) regions of interest (ROI) in the dispersion direction. We performed a $\Delta\chi^2$ analysis with 1 d.o.f., varying f_G. Key parameters of these fits are listed in Table 5. The resulting χ^2 values indicate good fits. The last column in Table 5, $P(\chi^2)$, tabulates the values of the cumulative χ^2 probability for the given degrees of freedom at the measured χ^2 value from the weighted fit residuals.

For the wide ROI [rows (a)–(c) in Table 5] the lowest χ^2 is at $f_G = 0$, or $R_g = \infty$ with 1σ errors in the 2 to 3 pixel range. For the narrow ROI [rows (d)–(f)], the χ^2 is smallest for f_G in the 2 to 3 pixel range, but 50%–75% errors. The two cases are consistent with one another, with the narrow ROI being less

Table 4. Ensemble Fit Parameter Summary[a]

Parameter	Table 5(a–f)	Table 6(a,b)	Description
Q_0	var	var	Signal floor
n	var	var	18th order Al normalization
f_G	var	var	Gaussian FWHM for 18th order
L	1.0	var	Fraction of nominal Al-Kα natural linewidth
S	1.0	var	Fraction of nominal Al-K$\alpha_{1,2}$ line separation
x_0	var	var	18th order Al-Kα_1 peak x position

[a]The list forms the set of parameters for Eq. (6). Fixed parameter values are listed in Column 2 for the fit cases defined in the table referenced in the top row.

Table 5. 18th Order Summary of Fits with Fixed Line Wavelengths and Widths[a]

Fit ID	CDB	ROI pixels	f_G pixels	R_g (90% l.l.) from $\Delta\chi^2$	R_g (90% l.l.) from fit	χ^2	DOF	$P(\chi^2)$
(a)	0	143	$0 + 2.8$	15600	-	125.0	135	0.28
(b)	$0, \pm1$	143	$0 + 1.8$	24500	-	133.6	135	0.48
(c)	$0, \pm1, \pm2$	143	$0 + 2.0$	21500	-	126.0	135	0.30
(d)	0	27	3.3 ± 1.8	9100	8700	20.55	19	0.64
(e)	$0, \pm1$	27	2.1 ± 1.5	12600	12200	16.76	19	0.39
(f)	$0, \pm1, \pm2$	27	2.6 ± 1.2	12100	12200	17.62	19	0.45

[a]Rows (a)–(c) had a wide ROI; (d)–(f) had a narrow ROI. Effective resolving power values, R_g, use dispersion distances D_{18}. (90% l.l.) means 90% probability that R_g is greater than the given value.

sensitive because it contains less information. The $\rho = 1$ fits, (a) and (d), had larger error due to lower count rates. In the rest of this work, we focus on analysis of $\rho = 3$ and 5 data. But, even from the data with the most counts [(b) and (c)], we cannot simply conclude the grating has better than 20000 effective resolving power because L is unknown at the 5% level and S is unknown at the 3% level, and these parameters are somewhat correlated with f_G.

Next, L and S are allowed to vary. Figure 17 compares best fit models for both $\rho = 3$ and 5 cases with data. We calculated $\Delta\chi^2$ over a 2D grid, varying the Gaussian FWHM, f_G, and the linewidth parameter L over specific grid values, while fitting the other parameters. Figure 18 shows the χ^2 probability contours for 2 deg of freedom. The contours indicate the range of acceptable values for L_{Al} with best case for $\rho = 5$ with a 1σ uncertainty of $^{-4\%}_{+2\%}$. The contours are consistent with the nominal 0.42 eV linewidth, with best fit at 98% of this value.

The first two columns in Table 6 show the key information from these fits. The χ^2 values suggest both are good fits. S errors were <1.5%.

The Column (b) result indicates that the grating effective resolving power lower limit is nearly 11000 at 95% confidence limit (c.l.), with $R_g = D_{18}/f_G$. The 90% c.l. value for $\rho = 5$ changed from 12100 to 11500, a 5% decrease, as a result of allowing the L and S to vary. This indicates that the data provides a robust measurement of the fit parameters.

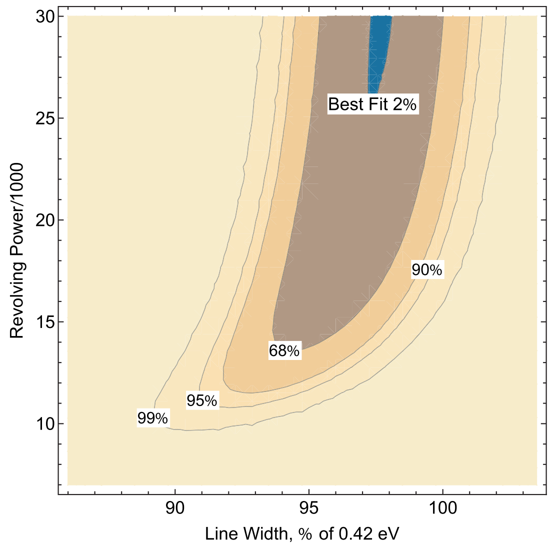

Fig. 18. Results of $\Delta\chi^2$ analysis for 18th order: Probability contours for $\rho = 5$ CDB case. The blue area represents the 2% probability around the best fit values. The value of 0.42 eV for the linewidth is taken from Table 2 [43].

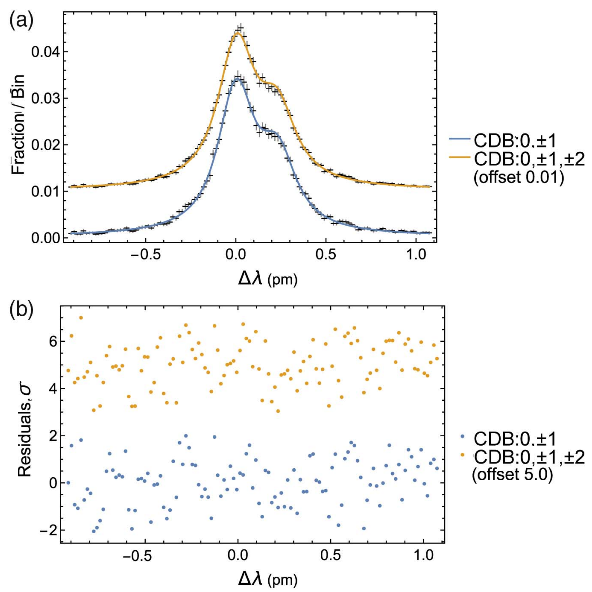

Fig. 17. 18th order Al best fit models, for three and five CDB cases compared with data. Key fit results are listed in Table 6 under fit IDs (a) and (b). $\Delta\lambda = 0$ corresponds to $\lambda = 833.95$ pm.

2. Other Al-K Orders

Profiles derived from deep integrations at Al 14th, 10th, and 7th orders were also fit with all parameter variables using the same model as the 18th order with the obvious adjustments. Key fit parameters are summarized for $\rho = 3$ under fit IDs (c), (e), and (g) in Table 6; 14th and 10th orders were also fit for $\rho = 5$ CDB cases, and fit parameters are summarized under fit IDs: (d) and (f) in Table 6. Results for these cases and the 18th order fits are in good agreement.

The Gaussian FWHM results are all consistent with the same value of approximately 2 pixels. Errors in f_G are generally large with the smallest ~30% for the 7th order. Possible implications of these results are further discussed in Section 5. Of course, the cases are not all independent because the $\rho = 5$ cases include the $\rho = 3$ data. The best fit values for L are consistent with one another as well as the nominal value. The best fit values for S are also consistent with one another but are generally less than 1 and, in the case of the 10th order,

Table 6. Variable Natural Linewidth Fit Summary[a]

Fit ID	(a)	(b)	(c)	(d)	(e)	(f)	(g)	(h)	(i)
Order	**18**	**18**	**14**	**14**	**10**	**10**	**7**	**18-14-10**	**18-14-10**
CDB	**0, ±1**	**0, ±1, ±2**	**0, ±1**	**0, ±1, ±2**	**0, ±1**	**0, ±1, ±2**	**0, ±1**	**0, ±1**	**0, ±1, ±2**
phot/1000	22.2	31.8	10.2	14.8	7.3	10.8	9.	39.7	57.4
f_G	2.58	2.03	2.64	1.93	2.07	1.96	2.39	2.86	2.02
σ_G	1.67	1.71	1.27	1.40	1.40	1.27	0.70	1.14	1.32
R_g (best fit)	18900	24000	14300	19600	13100	13800	7900	17000	24100
R_g (90% l.l. from fit)	9100	10000	8000	8900	6200	6700	5300	10300	11600
R_g (90% l.l. from $\Delta\chi^2$)	9800	11500	–	–	–	–	–	10400	12400
R_g (95% l.l. from fit)	8300	9000	7400	8100	5600	6100	5000	9600	10600
R_g (95% l.l. from $\Delta\chi^2$)	9500	10800	–	–	–	–	–	10000	11800
L	0.955	0.98	0.993	0.993	1.05	1.01	0.965	0.991	0.992
σ_L from fit	0.034	0.027	0.035	0.03	0.06	0.051	0.055	0.023	0.019
σ_L from $\Delta\chi^2$	0.04	+0.02, −0.04	–	–	–	–	–	0.03	0.02
S	0.995	0.974	0.959	0.971	0.921	0.911	0.931	0.969	0.969
σ_S	0.014	0.011	0.018	0.015	0.027	0.024	0.029	0.011	0.008
χ^2	107.6	95.5	141.9	133.7	63.0	61.4	42.8	329.0	311.6
DOF	107	107	123	119	56	53	48	292	287
$P(\chi^2\|\mathrm{DOF})$	0.53	0.22	0.88	0.83	0.76	0.80	0.31	0.93	0.85

[a]$(\sigma_G, \sigma_L, \sigma_S)$ are 1σ errors for (f_G, L, S). Effective resolving power values, R_g, use dispersion distance D_{18} for (a), (b), (h), and (i), D_{14} for (c) and (d), D_{10} for (e) and (f), and D_{07} for (g). Best fit model comparisons with data are not shown for all cases because of similarity with other fits. Best fit models are compared with data in Fig. 17 for (a), (b), and Fig. 19 for (i). $\Delta\chi^2$ analysis was not performed on cases (c)–(g). Probability contours are displayed for (b) in Fig. 18 and (i) in Fig. 20.

are significantly less than 1. The resolving power best fit values and lower limits decline with order because of the decreasing dispersion distance, since the best fit f_G and errors are relatively constant. Only the 7th order case excludes $R_g = \infty$ at a significant level. As expected, we are most sensitive to R_g at the higher orders, and the 18th order limits are the strongest constraint on $\Delta p/p$; the 14th and 10th order best fit f_G values still suggest high resolution, so we next describe a simultaneous fit of combined 18th, 14th, and 10th order data to check that the lower order results are consistent with the 18th order data and to try to achieve even better constraints on the fit parameters.

3. Ensemble Fitting of Al-K Orders

For the fit of the ensemble 18th, 14th, and 10th order Al data, each order was normalized independently. We used a single Gaussian FWHM parameter f_G but scaled by dispersion distance relative to 18th order for each order, i.e., $R_g = D_{18}/f_G$.

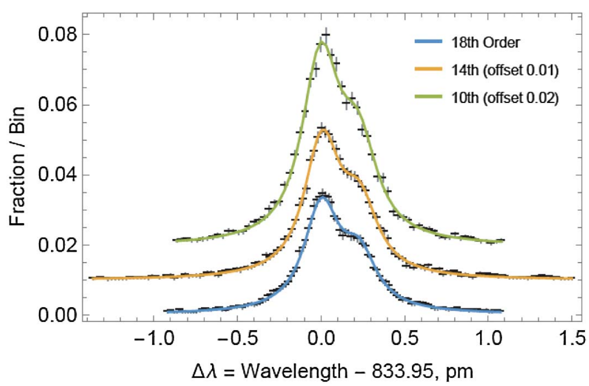

Fig. 19. Al (18th, 14th, 10th) combined best fit model for $\rho = 5$ case compared with data. Key fit results are listed in Table 6 under fit ID (i).

Figure 19 compares best fit models for the $\rho = 5$ case with data.

We again calculated $\Delta\chi^2$ over a 2D grid, varying f_G and L over specific grid values, while fitting the other parameters. Figure 20 shows the χ^2 probability contours for 2 deg of freedom. The five CDB case 95% c.l. contours indicate ∼20% higher resolving power lower limits, ∼12000, than $\rho = 3$, and ∼10% higher than the 18th order alone.

The contours indicate a narrower range of acceptable values for L than for the 18th order. The best case was for $\rho = 5$ with 2% 1σ uncertainty. The contours agree well with the nominal 0.42 eV linewidth, with best fit at 99% of this value.

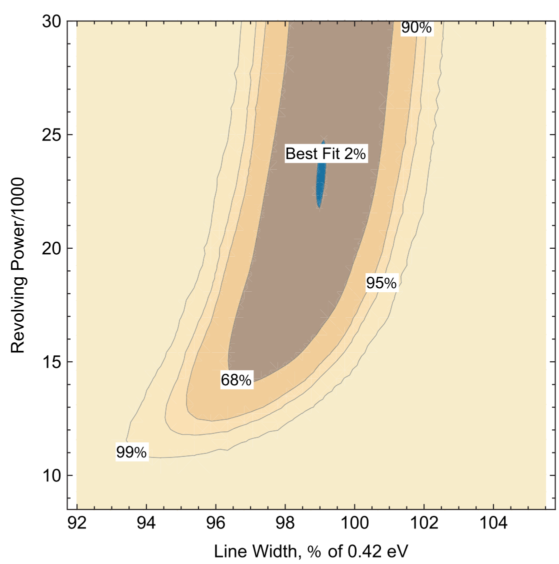

Fig. 20. Results of $\Delta\chi^2$ analysis for combined Al (18th, 14th, 10th) orders. Probability contours for $\rho = 5$ CDB case.

Table 7. Summary of Best Fit and Lower Limit Effective Resolving Power Results from the Most Sensitive Fit Cases[a]

Fit ID	Table 6(b)	Table 6(i)	(c)	(d)
Order	**18**	**Al-{18, 14, 10}**	**Al-{18, 14, 10}, Mg-12**	**Al-{18, 14, 10}, Mg-12**
CDB	**0, ±1, ±2**	**0, ±1, ±2**	**0, ±1**	**0, ±1, ±2**
R_g (best fit)	24000	24100	16400	23200
R_g (90% l.l. from fit)	10000	11600	10400	11700
R_g (90% l.l. from $\Delta\chi^2$)	11500	12400	12700	12300
R_g (95% l.l. from fit)	9000	10600	9700	10700
R_g (95% l.l. from $\Delta\chi^2$)	10800	11800	11800	11700

[a]The $\Delta\chi^2$ values account for asymmetries in the confidence level contours and, therefore, better reflect the true confidence levels.

This appears to be an improvement in precision over the best previously quoted uncertainty in the linewidth (see Section 5) [43].

The last two columns in Table 6 show information from these two fits. The χ^2 values suggest both are acceptable fits. The R_g values from the fit errors and the $\Delta\chi^2$ are in reasonable agreement, differing by <10% due to asymmetries in the $\Delta\chi^2$ contours. The fit parameter errors for L are consistent with those obtained from the $\Delta\chi^2$ contours, and S errors are slightly smaller than those attained from the 18th order alone, ∼1%.

The Column (i) result indicates that the grating effective resolving power lower limit is nearly 12000 at 95% c.l. This value is higher than that obtained with the 18th order alone, indicating that combining the three orders provides increased measurement sensitivity.

4. Ensemble Fitting of Mg-K and Al-K Orders

We also took data using a Mg anode, using the same procedures and data analysis approach. However, due to low flux and target contamination issues, these data were of limited value in trying to estimate R_g independently. We performed simultaneous fitting of Mg 12th and Al 18th, 14th, and 10th order data and varied the Gaussian FWHM, f_G, and the Mg linewidth parameter over specific grid values, while fitting most of the other parameters. Results for R_g (best fit, 90%, and 95% l.l.) were similar to Columns (h) and (i) in Table 6 and are summarized in Table 7.

5. Gratings X1 and X7

Images were also collected with the Al target for gratings X1 (7th, 10th, 14th, and 18th order) and X7 (7th and 10th order) for comparison with X4. The total counts are much lower due to shorter integration times, constraining the effective resolving power lower limits to values smaller than results for X4.

For comparison, identical orders from X1 and X7 are plotted on the same scale with X4 in Fig. 21. The profiles agree reasonably well.

We analyzed the 18th order X1 data in an abbreviated manner similar to X4. First holding the Lorentzian and separation parameters constant at the values determined for X4 ($L = 0.992$ and $S = 0.969$), we performed a 1D $\Delta\chi^2$ analysis. The fit result is shown in Fig. 22. Like X4, the result was consistent with $R_g = \infty$, with best fit $R_g = 14000$. Due to larger statistical errors, the 90% confidence lower limit was only 9000 compared with >12000 for X4 (see Table 5).

For the remaining X1 and X7 cases, we obtained 90% c.l. lower ($R_g = 3300 - 9000$) and upper limits ($R_g = 10600 - \infty$) along with best fit values ($R_g = 6400 - \infty$) from 1D $\Delta\chi^2$ in the same manner.

As expected, the 90% lower limits are not as constraining as X4 results due to the lower count numbers. However, the confidence intervals overlap among the gratings for each order. This suggests performance among gratings is consistent, even if we cannot obtain a lower limit $R_g > 10000$ for X1 and X7 because of limited counting statistics.

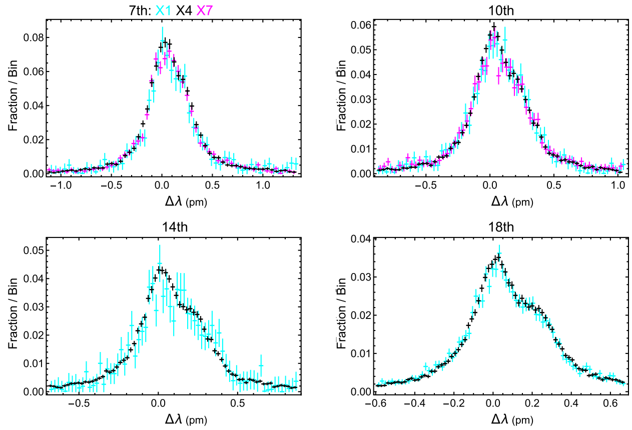

Fig. 21. Al 7th, 10th, 14th, and 18th line profile comparison among gratings. 7th and 10th order X4 (black) profiles are compared with X7 (magenta) and X1 (cyan) in the top panels. 14th and 18th order X4 profiles are compared with only X1 in the bottom panels. X7 efficiency was too low above 10th order to justify measurements.

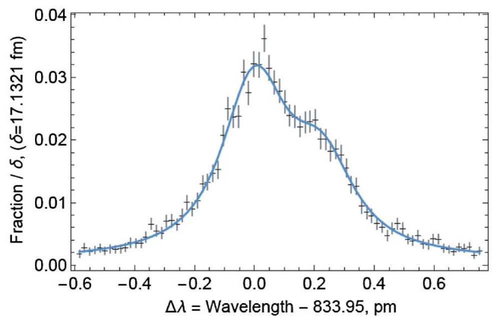

Fig. 22. 18th order Al best fit models for X1 grating using five CDB, compared with data. Line wavelengths and widths were fixed at 0.992 and 0.969 of their nominal values.

5. DISCUSSION

We conclude that the above results constrain the CAT grating effective resolving power above 11000 at 95% confidence for X4. The most constraining single order was the 18th order using CDB: $0, \pm 1, \pm 2$ [Table 6(b)] with R_g (95% l.l. from $\Delta\chi^2$) $=10800$. We found that combining Al results from the 18th, 14th, and 10th order [Table 6(i)] increased this limit to 11800. While spectral contamination and lower counting rates limited Mg data, combining the aforementioned Al orders with Mg 12th order data yielded a comparable R_g lower limit. Best fit and lower limit values are summarized in Table 7.

All of the other fits were consistent with these, in that lower sensitivity was the result of poorer statistics or lower dispersion. All the cases were consistent with no grating contribution (∞ effective resolving power) at the 90% c.l. (upper limit) except for 7th order Al. Of course, $R_g = \infty$ is only meaningful in the mathematical sense of our definition of $R_g = p/\Delta p$. We neglect here that the resolving power is always limited by the number of illuminated grating periods times the diffraction order. However, even for just 1 mm of illuminated width, $p = 200$ nm, and $m = 18$, this limit would mean $R < 90000$, which is practically indistinguishable from $R_g = \infty$ in our analysis.

Independent of x-ray data taken at the SLTF, we have knowledge of certain properties of the three tested CAT gratings that should be considered when discussing the above results.

A. Known Blaze Angle Variation

Three effects have an impact on what fraction of the area of a grating in our tests contributes efficiently to each diffraction peak.

First, recent measurements using small-angle x-ray scattering (SAXS) have shown that our current DRIE tool produces deep etches with a small but significant and systematic variation in etch angle across the surface of a 30 mm grating [45]. This produces grating bars that are inclined relative to each other. This means that, for any given orientation of the grating surface normal, grating bar sidewalls will be oriented at a range of angles to the incident x rays. Thus, some areas of the grating will be at the most favorable angle for blazing into the mth order, while others will not. For X4, we estimate from our efficiency models [20,26] that the range of contributing angles is 0.65 (7th order), 0.5 (10th order), 0.3 (14th order), and 0.25 deg (18th order). The range becomes smaller due to the decreasing grating bar sidewall reflectivity with increasing α. This translates into an area of 13 (7th order), 10 (10th order), 6 (14th order), and 5 mm (18th order) in length along the dispersion direction contributing to the given orders. Recent testing with a more modern DRIE tool [46] has produced CAT grating geometry etches with significantly smaller etch angle variations [47].

Second, the gratings sit in a converging beam. Over 30 mm in azimuth, the incident angle varies by ~0.19 deg. In the mounted orientation (grating device layer facing the source), this effect runs in the opposite direction of the first effect, leading to a slight narrowing of the expected contributing areas.

Third, the gratings are not perfectly flat. We observe a slight “dimpling” or “buckling” of the device layer within many L2 hexagons. This effect amounts to a broadening of the blaze angle distribution across a hexagon, thus negating to some degree the impacts of the first two effects and increasing the range of areas contributing to a given diffraction peak. Based on SAXS, white light interferometry [48], and reflection measurements [49], we estimate that this effect extends the range of contributing areas by 5 to 10 mm.

B. Known Grating Period Variation

The gratings in this study were patterned using the optical interference of two mutually coherent spherical waves [50]. This creates a grating pattern with well-understood hyperbolic distortions and period distribution. We can calculate this (non-Gaussian) period distribution from the geometric parameters of our interference lithography station and derive an upper limit for the resolving power. If we consider the period distribution over a (30×4) mm^2 area in the center of the interference pattern, we obtain $R_g = 26900$ as an upper limit. If the interference pattern was off-center by 4 mm from the grating center (a reasonable possibility given our current procedures), the upper limit reduces to 18700. Thus, even though the period distribution due to hyperbolic distortions is non-Gaussian, it is too narrow to have a noticeable impact on our effective resolving power modeling results. In addition, period variations over the smaller areas that effectively contribute to the individual orders (see previous paragraph) are even smaller and can thus be safely ignored. For future, much larger gratings, there are alternative patterning techniques that do not suffer from hyperbolic distortions [51].

C. Diffraction from the L1 Cross Support Mesh

The 5 μm period L1 cross support mesh is a periodic structure with a grating vector nominally perpendicular to the grating vector for the 200 nm period CAT grating bars. As a periodic structure, it will also cause diffraction peaks but in the direction along its own grating vector. At each CAT grating diffraction order, we would therefore expect first-order Al-K peaks from the L1 mesh at ± 114 pixels in the cross-dispersion (y) direction. Diffraction by the L1 mesh is expected to be weak due to the large L1 period (relative to the wavelength) and the small fraction of the period being taken up by the L1 bars. In the analysis presented here, $\pm$1st order L1 peaks could potentially affect the outermost CDBs weakly if the L1 grating vector is not parallel to the y direction (for example, due to limited precision in the patterning steps during fabrication). In other scenarios, these peaks are more readily identifiable [26].

D. Estimating Period Distribution through Deconvolution

To check if the grating response was significantly non-Gaussian within our measurement resolution, we performed a Richardson–Lucy deconvolution on the Al 18th order measured line profiles, using the best fit line profile without Gaussian broadening. Under the assumption that the grating contribution is produced only by period variations, $\Delta p/p$, we can interpret the deconvolved profile as a distribution of periods relative to the nominal 200 nm. Figure 23 shows that the deconvolved grating contribution has the most power constrained to two adjacent bins, which is consistent with an effective resolving power of 25000. While Gaussian FWHM

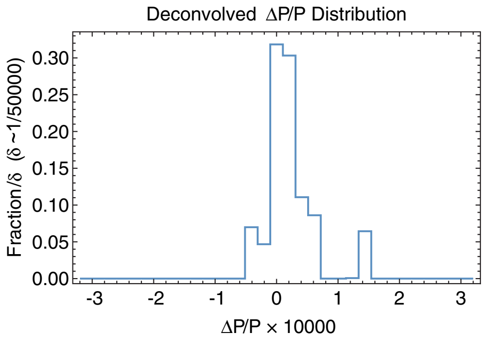

Fig. 23. Distribution of period errors from deconvolution. Result is based on a Richardson–Lucy deconvolution of 18th order Al data within the central five CDBs using the best fit line model convolved with zero order as the deconvolution kernel. The deconvolution was iterated until the variance between the reconvolved and measured profiles was minimized.

errors were almost always large compared with the best fit value, we did find that the best fit values consistently fell between two and three pixels regardless of order. This might imply that the grating-induced broadening is not dominated by $\Delta p/p$ (which scales with dispersion distance). For example, if the L1 support structure is misaligned from the normal to the CAT grating bars, and cross-dispersion efficiency differs between zero order and other orders, then there could be a contribution that does not scale with dispersion and is not accounted for by the zero order. Because the test was performed with an essentially unfiltered Al spectrum, the cross-dispersion spectrum from the zero order should contain all the continuum and low-level contaminant lines, whereas the cross-dispersion at dispersed orders should contain only Al-K lines. Thus, even if there is no cross-dispersion efficiency difference between zero order and other orders, there could still be a difference between the zero and dispersed order LRFs. Alternatively, there could be unknown systematic effects.

E. Improved Al-*K* Doublet Parameter Uncertainties

The Al-*K* linewidth and separation parameters were best constrained by the combined Al 18th/14th/10th orders using CDB: $0, \pm 1, \pm 2$ at 0.992 ± 0.019, and 0.969 ± 0.008, respectively. These correspond to 0.417 ± 0.008 eV or 231.6 ± 4.6 fm for the linewidth and 0.400 ± 0.003 eV or 224.4 ± 1.8 fm for the line separation. The linewidth includes uncertainty due to the zero-order width uncertainty of 1.2 fm or 0.002 eV. The separation uncertainty is a factor of 3 smaller than the value quoted in [7], and the linewidth uncertainty is a factor of 2.5 smaller than the value quoted in [43].

We made the following assumptions in the interpretation of the fit results:

1) We assumed a Gaussian response to account for the dispersed grating contribution;
2) the natural line shape is a pure Lorentzian function;
3) the convolution of the natural line shapes with the zero-order response function represents the predicted response from a grating with $R_g = \infty$;
4) Broadening in the dispersed profile is assumed to be a measure of $\Delta p/p$ errors in the gratings.

The strongest and only result contradicting the $\Delta p/p$ assumption is 7th order Al, which indicates a $>3\sigma$ detection of a 2.4 pixel FWHM Gaussian contribution in the dispersed profile. Scaling, this would imply a 6.2 pixel FWHM at the 18th order or $R_g \approx 8000$, which is excluded at >99% c.l. On the other hand, effective resolving powers of $\{11000, 20000\}$ at the 18th order, would suggest Gaussian FWHMs of $\{1.7, 1.0\}$ pixels, which are only $\{1.0\sigma, 2.0\sigma\}$ from the best fit value for the 7th order. Thus, even the 7th order measurement is reasonably consistent with the other results.

6. SUMMARY AND CONCLUSIONS

We assembled a breadboard prototype for a CAT grating-based x-ray spectrometer, consisting of a grazing incidence Wolter-I mirror pair (TDM) and 30 mm wide CAT gratings. The TDM was illuminated with x rays from an electron impact source with Al and Mg targets at a distance of 92.17 m. The convolution of slit-limited source, TDM PSF, and CCD pixelation provided an anisotropic focal spot with 0.9 arcsec FWHM in the horizontal direction.

Zeroth order line profiles (with a grating moved into the beam) only showed weakly increased scatter compared with the unobstructed line profile, thus demonstrating minimal changes in the PSF due to the gratings. We developed an empirical line response function model for the zeroth order for convolution with the spectrum of the characteristic Al-K_α doublet. Measured values from the literature were used as reference parameters for the doublet. The resulting modeled response served as a prediction for the measured diffracted line profile. We assumed any additional broadening to be due to grating period variations and modeled this effect as an additional convolution with a Gaussian with FWHM of f_G. Gratings with period variation width f_G would limit resolving power of the measurement to $R_g = D_m/f_G$. Fits to our data up to the 18th order for Al-K consistently produced $R_g > 11000$ at 95% confidence for grating X4 and best fit values in the range of $R_g \sim 16000$–24000.

For the 18th order, the maximum resolving power R_{XGS} for the spectrometer could be ~24000, only utilizing the central three CDBs and assuming no broadening due to the grating. Taking the deduced grating contribution into account from Column (c) in Table 7, for example, we arrive at an experimentally demonstrated 90% confidence level lower limit for the resolving power of $R_{\mathrm{XGS}} \sim 11200$ for the presented breadboard grating spectrometer.

Fits to data from gratings X1 and X7 were consistent with the results from X4 but produced lower constraints on R_g due to shorter integration times and, therefore, lower counting statistics. Within measurement uncertainty, the three independently fabricated gratings provide the same resolving power in a given diffraction order, lending confidence to the repeatability of the fabrication process.

The best constraints often resulted in values for the relative Al-K linewidth and separation parameters to be slightly less than one. The 1σ uncertainties usually include the value 1 for the linewidth parameter but slightly less so for the separation parameter. The smaller uncertainties, compared with literature values, indicate that the spectrometer setup in this work provides superior resolving power compared with a soft x-ray double-crystal spectrometer. This performance might inspire new high-resolution spectrometer designs for laboratory-based plasma and astrophysics studies.

Our results demonstrate that CAT gratings are compatible with XGS designs with resolving power $R_{\mathrm{XGS}} > 10000$. The relaxed alignment and figure requirements in the transmission geometry tolerate many micrometers of nonflatness in the grating membranes and many arcminutes of misalignment for most rotational degrees of freedom, which reduce constraints on fabrication, alignment, and mounting. CAT gratings have passed environmental testing for launch vibrations and temperature cycling under vacuum without performance degradation, and grating-to-grating roll alignment to within 5 arcmin has been demonstrated [26,52]. Significant gains in diffraction efficiency are possible from CAT gratings with deeper (~6 μm) grating bars [53]. CAT gratings are therefore promising diffraction gratings for space-based soft x-ray spectrometers with high resolving power and large collecting area, and they can easily meet requirements for the *Arcus Explorer* mission ($R_{\mathrm{XGS}} > 2500$) currently undergoing a NASA Phase A study [1,52].

Funding. National Aeronautics and Space Administration (NASA) (NNX15AC43G).

Acknowledgment. We like to express our gratitude to W. Zhang, R. McClelland, K.-W. Chan, J. Niemeyer, and M. Schofield from the Next-Generation X-ray Optics group at the NASA Goddard Space Flight Center for supplying the TDM, to S. O'Dell (NASA Marshall Space Flight Center) for helpful discussions, to R. Bhatia (Veeco-CNT) for ALD coating of the CAT gratings, and to J. Song (MIT) for SAXS measurements.

REFERENCES

1. R. K. Smith, M. Abraham, R. Allured, M. Bautz, J. Bookbinder, J. Bregman, L. Brenneman, N. S. Brickhouse, D. Burrows, V. Burwitz, P. N. Cheimets, E. Costantini, S. Dawson, C. DeRoo, A. Falcone, A. R. Foster, L. Gallo, C. Grant, H. M. Günther, R. K. Heilmann, E. Hertz, B. Hine, D. Huenemoerder, J. S. Kaastra, I. Kreykenbohm, K. K. Madsen, R. McEntaffer, E. Miller, J. Miller, E. Morse, R. Mushotzky, K. Nandra, M. Nowak, F. Paerels, R. Petre, K. Poppenhaeger, A. Ptak, P. Reid, J. Sanders, M. Schattenburg, N. Schulz, A. Smale, P. Temi, L. Valencic, S. Walker, R. Willingale, J. Wilms, and S. J. Wolk, "Arcus: exploring the formation and evolution of clusters, galaxies, and stars," Proc. SPIE **10397**, 103970Q (2017).
2. J. A. Gaskin, R. Allured, S. R. Bandler, S. Basso, M. W. Bautz, M. F. Baysinger, M. P. Biskach, T. M. Boswell, P. D. Capizzo, K.-W. Chan, M. M. Civitani, L. M. Cohen, V. Cotroneo, J. M. Davis, C. T. DeRoo, M. J. DiPirro, A. Dominguez, L. L. Fabisinski, A. D. Falcone, E. Figueroa-Feliciano, J. C. Garcia, K. E. Gelmis, R. K. Heilmann, R. C. Hopkins, T. Jackson, K. Kilaru, R. P. Kraft, T. Liu, R. S. McClelland, R. L. McEntaffer, K. S. McCarley, J. A. Mulqueen, F. Özel, G. Pareschi, P. B. Reid, R. E. Riveros, M. A. Rodriguez, J. W. Rowe, T. T. Saha, M. L. Schattenburg, A. R. Schnell, D. A. Schwartz, P. M. Solly, R. M. Suggs, S. G. Sutherlin, D. A. Swartz, S. Trolier-McKinstry, J. H. Tutt, A. Vikhlinin, J. Walker, W. Yoon, and W. W. Zhang, "Lynx mission concept status," Proc. SPIE **10397**, 103970S (2017).
3. K. D. Irwin and G. C. Hilton, "Transition-edge sensors," in *Cryogenic Particle DetectionTopics in Applied Physics* (2005), Vol. **99**, pp. 63–150.
4. S. J. Lee, J. S. Adams, S. R. Bandler, J. A. Chervenak, M. E. Eckart, F. M. Finkbeiner, R. L. Kelley, C. A. Kilbourne, F. S. Porter, J. E. Sadleir, S. J. Smith, and E. J. Wassell, "Fine pitch transition-edge sensor X-ray microcalorimeters with sub-eV energy resolution at 1.5 keV," Appl. Phys. Lett. **107**, 223503 (2015).
5. C. R. Canizares, J. E. Davis, D. Dewey, K. A. Flanagan, E. B. Galton, D. P. Huenemoerder, K. Ishibashi, T. H. Markert, H. L. Marshall, and M. McGuirk, "The Chandra high-energy transmission grating: design, fabrication, ground calibration, and 5 years in flight," Publ. Astron. Soc. Pac. **117**, 1144–1171 (2005).
6. J. W. den Herder, A. C. Brinkman, S. M. Kahn, G. Branduardi-Raymont, K. Thomsen, H. Aarts, M. Audard, J. V. Bixler, A. J. den Boggende, J. Cottam, T. Decker, L. Dubbeldam, C. Erd, H. Goulooze, M. Güdel, P. Guttridge, C. J. Hailey, K. Al Janabi, J. S. Kaastra, P. A. J. de Korte, B. J. van Leeuwen, C. Mauche, A. J. McCalden, R. Mewe, A. Naber, F. B. Paerels, J. R. Peterson, A. P. Rasmussen, K. Rees, I. Sakelliou, M. Sako, J. Spodek, M. Stern, T. Tamura, J. Tandy, C. P. de Vries, S. Welch, and A. Zehnder, "The reflection grating spectrometer on board XMM-Newton," Astron. Astrophys. **365**, L7–L17 (2001).
7. J. Schweppe, R. D. Deslattes, T. Mooney, and C. J. Powell, "Accurate measurement of Mg and A1 $K\alpha_{1,2}$ X-ray energy profiles," J. Electron. Spectrosc. Relat. Phenom. **67**, 463–478 (1994).
8. P. Beiersdorfer, J. R. Crespo López-Urrutia, E. Förster, J. Mahiri, and K. Widmann, "Very high resolution soft x-ray spectrometer for an electron beam ion trap," Rev. Sci. Instrum. **68**, 1077–1079 (1997).
9. K. Widmann, P. Beiersdorfer, G. V. Brown, J. R. Crespo López Urrutia, V. Decaux, and D. W. Savin, "A high-resolution transmission-type x-ray spectrometer designed for observation of the Kα transitions of highly charged high-Z ions," Rev. Sci. Instrum. **68**, 1087–1090 (1997).
10. Y. Yang, J. Xiao, D. Lu, Y. Shen, K. Yao, C. Chen, R. Hutton, and Y. Zou, "A high precision flat crystal spectrometer compatible for ultra-high vacuum light source," Rev. Sci. Instrum. **88**, 113108 (2017).
11. P. Beiersdorfer and E. Träbert, "High-resolution laboratory measurements of coronal lines near the Fe IX line at 171Å," Astrophys. J. **854**, 114 (2018).
12. G. Ghiringhelli, A. Piazzalunga, C. Dallera, G. Trezzi, L. Braicovich, T. Schmitt, V. N. Strocov, R. Betemps, L. Patthey, X. Wang, and M. Grioni, "SAXES, a high resolution spectrometer for resonant x-ray emission in the 400–1600 eV energy range," Rev. Sci. Instrum. **77**, 113108 (2006).
13. V. N. Strocov, T. Schmitt, U. Flechsig, T. Schmidt, A. Imhof, Q. Chen, J. Raabe, R. Betemps, D. Zimoch, J. Krempasky, X. Wang, C. M. Grioni, A. Piazzalungaa, and L. Patthey, "High-resolution soft X-ray beamline ADRESS at the swiss light source for resonant inelastic X-ray scattering and angle-resolved photoelectron spectroscopies," J. Synchrotron Radiat. **17**, 631–643 (2010).
14. Y. Harada, M. Kobayashi, H. Niwa, Y. Senba, H. Ohashi, T. Tokushima, Y. Horikawa, S. Shin, and M. Oshima, "Ultrahigh resolution soft x-ray emission spectrometer at BL07LSU in SPring-8," Rev. Sci. Instrum. **83**, 013116 (2012).
15. T. Warwick, Y.-D. Chuang, D. L. Voronov, and H. A. Padmore, "A multiplexed high-resolution imaging spectrometer for resonant inelastic soft X-ray scattering spectroscopy," J. Synchrotron Rad. **21**, 736–743 (2014).
16. R. Qiao, Q. Li, Z. Zhuo, S. Sallis, O. Fuchs, M. Blum, L. Weinhardt, C. Heske, J. Pepper, M. Jones, A. Brown, A. Spucces, K. Chow, B. Smith, P.-A. Glans, Y. Chen, S. Yan, F. Pan, L. F. J. Piper, J. Denlinger, J. Guo, Z. Hussain, Y.-D. Chuang, and W. Yang, "High-efficiency in situ resonant inelastic x-ray scattering (iRIXS) endstation at the advanced light source," Rev. Sci. Instrum. **88**, 033106 (2017).
17. M. M. Sala, K. Martel, C. Henriquet, A. Al Zein, L. Simonelli, Ch. J. Sahle, H. Gonzalez, M.-C. Lagier, C. Ponchut, S. Huotari, R. Verbeni, M. Krisch, and G. Monaco, "A high-energy-resolution resonant inelastic x-ray scattering spectrometer at ID20 of the European synchrotron radiation facility," J. Synchrotron Radiat. **25**, 580–591 (2018).
18. R. K. Heilmann, J. E. Davis, D. Dewey, M. W. Bautz, R. Foster, A. Bruccoleri, P. Mukherjee, D. Robinson, D. P. Huenemoerder, H. L. Marshall, M. L. Schattenburg, N. S. Schulz, L. J. Guo, A. F. Kaplan, and R. B. Schweikart, "Critical-angle transmission grating

spectrometer for high-resolution soft x-ray spectroscopy on the International X-Ray Observatory," Proc. SPIE **7732**, 77321J(2010).
19. H. M. Günther, R. K. Heilmann, P. Cheimets, and R. K. Smith, "Performance of a double tilted-Rowland-spectrometer on Arcus," Proc. SPIE **10397**, 103970P (2017).
20. R. K. Heilmann, M. Ahn, A. Bruccoleri, C.-H. Chang, E. M. Gullikson, P. Mukherjee, and M. L. Schattenburg, "Diffraction efficiency of 200 nm period critical-angle transmission gratings in the soft x-ray and extreme ultraviolet wavelength bands," Appl. Opt. **50**, 1364–1373 (2011).
21. C.-H. Chang, J. C. Montoya, M. Akilian, A. Lapsa, R. K. Heilmann, M. L. Schattenburg, M. Li, K. A. Flanagan, A. P. Rasmussen, J. F. Seely, J. M. Laming, B. Kjornrattanawanich, and L. I. Goray, "High fidelity blazed grating replication using nanoimprint lithography," J. Vac. Sci. Technol. B **22**, 3260–3264 (2004).
22. J. F. Seely, L. I. Goray, B. Kjornrattanawanich, J. M. Laming, G. E. Holland, K. A. Flanagan, R. K. Heilmann, C.-H. Chang, M. L. Schattenburg, and A. P. Rasmussen, "Efficiency of a grazing incidence off-plane grating in the soft X-ray region," Appl. Opt. **45**, 1680–1687 (2006).
23. R. McEntaffer, C. DeRoo, T. Schultz, B. Gantner, J. Tutt, A. Holland, S. O'Dell, J. Gaskin, J. Kolodziejczak, W. W. Zhang, K.-W. Chan, M. Biskach, R. McClelland, D. Iazikov, X. Wang, and L. Koecher, "First results from a next-generation off-plane X-ray diffraction grating," Exp. Astron. **36**, 389–405 (2013).
24. B. D. Donovan, R. L. McEntaffer, J. H. Tutt, C. T. DeRoo, R. Allured, J. A. Gaskin, and J. J. Kolodziejczak, "X-ray verification of an optically aligned off-plane grating module," Appl. Opt. **57**, 454–464 (2018).
25. R. K. Heilmann, M. Ahn, E. M. Gullikson, and M. L. Schattenburg, "Blazed high-efficiency x-ray diffraction via transmission through arrays of nanometer-scale mirrors," Opt. Express **16**, 8658–8669 (2008).
26. R. K. Heilmann, A. R. Bruccoleri, J. Song, J. Kolodziejczak, J. A. Gaskin, S. L. O'Dell, P. Cheimets, E. Hertz, R. K. Smith, V. Burwitz, G. Hartner, M.-M. La Caria, and M. L. Schattenburg, "Critical-angle transmission grating technology development for high resolving power soft X-ray spectrometers on Arcus and Lynx," Proc. SPIE **10399**, 1039914 (2017).
27. J. E. Davis, M. W. Bautz, D. Dewey, R. K. Heilmann, J. C. Houck, D. P. Huenemoerder, H. L. Marshall, M. A. Nowak, M. L. Schattenburga, N. S. Schulz, and R. Smith, "Raytracing with MARX—X-ray observatory design, calibration, and support," Proc. SPIE **8443**, 84431A (2012).
28. M. W. Bautz, W. C. Cash, J. E. Davis, R. K. Heilmann, D. P. Huenemoerder, M. L. Schattenburg, R. McEntaffer, R. Smith, S. J. Wolk, W. W. Zhang, S. P. Jordan, and C. F. Lillie, "Concepts for high-performance soft x-ray grating spectroscopy in a moderate-scale mission," Proc. SPIE **8443**, 844315 (2012).
29. H. M. Günther, M. W. Bautz, R. K. Heilmann, D. P. Huenemoerder, H. L. Marshall, M. A. Nowak, and N. S. Schulz, "Ray-tracing critical-angle transmission gratings for the X-ray surveyor and explorer-size missions," Proc. SPIE **9905**, 990556 (2016).
30. H. M. Günther and R. K. Heilmann, "An x-ray transmission grating spectrometer for Lynx," Proc. SPIE **10699**, 1069914 (2018).
31. M. P. Biskach, K.-W. Chan, J. R. Mazzarella, R. S. McClelland, T. T. Saha, M. J. Schofield, and W. W. Zhang, "Alignment and integration of thin, lightweight x-ray optics into modules," Proc. SPIE **9144**, 914446 (2014).
32. A. R. Bruccoleri, R. K. Heilmann, and M. L. Schattenburg, "Fabrication process for 200 nm-pitch polished freestanding ultra-high aspect ratio gratings," J. Vac. Sci. Technol. B **34**, 06KD02 (2016).
33. A. R. Bruccoleri, D. Guan, P. Mukherjee, R. K. Heilmann, and M. L. Schattenburg, "Potassium hydroxide polishing of nanoscale deep reactive-ion etched ultra-high aspect ratio gratings," J. Vac. Sci. Technol. B **31**, 06FF02 (2013).
34. A. R. Bruccoleri, D. Guan, R. K. Heilmann, S. Vargo, F. DiPiazza, and M. L. Schattenburg, "Nanofabrication advances for high efficiency critical-angle transmission gratings," Proc. SPIE **8861**, 886119 (2013).
35. A. Bruccoleri, P. Mukherjee, R. K. Heilmann, J. Yam, and M. L. Schattenburg, "Fabrication of nanoscale, high throughput, high aspect ratio freestanding gratings," J. Vac. Sci. Technol. B **30**, 06FF03 (2012).
36. M. Ahn, R. K. Heilmann, and M. L. Schattenburg, "Fabrication of ultrahigh aspect ratio freestanding gratings on silicon-on-insulator wafers," J. Vac. Sci. Technol. B **25**, 2593–2597 (2007).
37. W. C. Cash, Jr., "X-ray optics 2: a technique for high-resolution spectroscopy," Appl. Opt. **30**, 1749–1759 (1991).
38. J. J. Kolodziejczak, S. L. O'Dell, R. F. Elsner, and M. C. Weisskopf, "Evidence for dust contamination on the VETA-1 mirror surface," Proc. SPIE **1742**, 162–170 (1992).
39. S. L. O'Dell, R. F. Elsner, J. J. Kolodziejczak, M. C. Weisskopf, J. P. Hughes, and L. P. van Speybroeck, "X-ray evidence for particulate contamination on the AXAF VETA-1 mirrors," Proc. SPIE **1742**, 171–182 (1992).
40. R. K. Heilmann, M. Ahn, M. W. Bautz, R. Foster, D. P. Huenemoerder, H. L. Marshall, P. Mukherjee, M. L. Schattenburg, N. S. Schulz, and M. Smith, "Development of a critical-angle transmission grating spectrometer for the International X-ray observatory," Proc. SPIE **7437**, 74370G (2009).
41. J. A. Bearden and A. F. Burr, "Reevaluation of x-ray atomic energy levels," Rev. Mod. Phys. **39**, 78–124 (1967).
42. W. L. Baun and D. W. Fischer, "The effect of chemical combination on K x-ray emission spectra from magnesium, aluminum and silicon," Technical Report AFML-TR-64-350 (Air Force Materials Laboratory, 1964).
43. J. L. Campbell and T. Papp, "Widths of the atomic K-N7 levels," At. Data Nucl. Data Tables **77**, 1–56 (2001).
44. M. O. Krause and J. H. Oliver, "Natural widths of atomic K and L levels, Kα x-ray lines and several KLL Auger lines," J. Phys. Chem. Ref. Data **8**, 329–338 (1979).
45. J. Song, R. K. Heilmann, A. R. Bruccoleri, E. Hertz, and M. L. Schattenburg, "Metrology for quality control and alignment of CAT grating spectrometers," Proc. SPIE **10699**, 106990S (2018).
46. R. Barnett, D. Thomas, Y. Song, D. Tossell, T. Barrass, and O. Ansell, "A new plasma source for next generation MEMS deep Si etching: Minimal tilt, improved profile uniformity and higher etch rates," in *60th Electronic Components and Technology Conference (ECTC)* (2010), pp. 1056–1059.
47. J. Song, A. R. Bruccoleri, R. K. Heilmann, J. Scholvin, and M. L. Schattenburg, "High-precision x-ray metrology for characterization of bar tilt in nanoscale x-ray gratings," in preparation.
48. R. K. Heilmann, A. R. Bruccoleri, and M. L. Schattenburg, "High-efficiency blazed transmission gratings for high-resolution soft x-ray spectroscopy," Proc. SPIE **9603**, 960314 (2015).
49. J. Song, R. K. Heilmann, A. R. Bruccoleri, E. Hertz, and M. L. Schattenburg, "Scanning laser reflection tool for alignment and period measurement of critical-angle transmission gratings," Proc. SPIE **10399**, 1039915 (2017).
50. J. Ferrera, M. L. Schattenburg, and H. I. Smith, "Analysis of distortion in interferometric lithography," J. Vac. Sci. Technol. B **14**, 4009–4013 (1996).
51. R. K. Heilmann, C. G. Chen, P. T. Konkola, and M. L. Schattenburg, "Dimensional metrology for nanometer-scale science and engineering: towards sub-nanometer accurate encoders," Nanotechnology **15**, S504 (2004).
52. R. K. Heilmann, A. R. Bruccoleri, J. Song, C. deRoo, P. Cheimets, E. Hertz, R. K. Smith, V. Burwitz, G. Hartner, M.-M. La Caria, C. Pelliciari, H. M. Günther, S. N. T. Heine, B. LaMarr, H. L. Marshall, N. S. Schulz, E. M. Gullikson, and M. L. Schattenburg, "Blazed transmission grating technology development for the Arcus x-ray spectrometer explorer," Proc. SPIE **10699**, 106996D (2018).
53. R. K. Heilmann, A. R. Bruccoleri, J. Kolodziejczak, J. A. Gaskin, S. L. O'Dell, R. Bhatia, and M. L. Schattenburg, "Critical-angle x-ray transmission grating spectrometer with extended bandpass and resolving power >10,000," Proc. SPIE **9905**, 99051X (2016).